Asymmetric stacking patch for debonding suppression in single-sided patch repair of composite structures

Hashimoto, Kohei
Department of Aeronautics and Astronautics, Kyushu University

Yashiro, Shigeki
Department of Aeronautics and Astronautics, Kyushu University

Onodera, Sota
Department of Aeronautics and Astronautics, Kyushu University

Ryuzono, Kazuki
Department of Aerospace Engineering, Tohoku University

https://hdl.handle.net/2324/7358021

出版情報：Composite Structures. 355, pp.118843-, 2025-02. Elsevier
バージョン：

Composite Structures 355 (2025) 118843

Contents lists available at ScienceDirect

Composite Structures

journal homepage: www.elsevier.com/locate/compstruct

Asymmetric stacking patch for debonding suppression in single-sided patch repair of composite structures

Kohei Hashimoto [a], Shigeki Yashiro [a,*], Sota Onodera [a], Kazuki Ryuzono [b]

[a] Department of Aeronautics and Astronautics, Kyushu University, 744 Motooka, Nishi-ku, Fukuoka 819-0395, Japan

[b] Department of Aerospace Engineering, Tohoku University, 6-6-01, Aoba, Aramaki, Aoba-ku, Sendai, Miyagi 980-8579, Japan

ARTICLE INFO

Keywords:
Composite patch
Joints/joining
Stacking sequence optimization
Tensile-bending coupling
Debonding

ABSTRACT

With the increasing use of composite structures, a simple and effective repair method is needed to enhance operational efficiency. While conventional single-sided patch repairs are straightforward, they are prone to debonding due to secondary bending deformation, leading to low post-repair strength. This study proposes a single-sided patch with an asymmetric lay-up designed to suppress debonding by utilizing coupled tensile-bending deformation. The stacking sequence of the patches was optimized using a genetic algorithm to minimize the adhesive's expansion strain energy density. The optimal stacking sequence generates bending deformation with curvature opposite to the secondary bending observed under tensile loading in a patch-repaired plate. This discrepancy in bending deformation alleviates the hydrostatic stress in the adhesive at the patch edges and reduces the contribution of Mode I to patch debonding. Tensile tests using optimized patches demonstrated the debonding suppression mechanism, showing that the onset strain for debonding improved due to material failure occurring in the base CFRP laminate.

1. Introduction

In recent years, the use of carbon fiber reinforced polymers (CFRPs) in primary aircraft structures has expanded, leading to increased demand for simple repair methods to address in-service structural damage [1]. Currently, scarf joints are the most common method for repairing CFRP structures [2]. Scarf repairs offer high repair effectiveness and a flush aerodynamic surface post-repair, resulting in excellent aerodynamic properties [3]. However, the process is cumbersome and time-consuming, reducing aircraft operational efficiency [4,5].

In contrast, patch repair is a simpler method, where a prepared CFRP patch is adhered to the damaged area using adhesive. While the post-repair strength of patch repairs is lower than that of scarf repairs, patch repairs are effective for temporary fixes due to operational constraints [6,7]. Over the past several decades, numerous studies have been conducted on double-sided patch repairs, focusing on the effects of patch geometry on post-repair strength [8–14]. However, double-sided patch repairs cannot be applied to areas where the interior is structurally inaccessible, such as the boundary of the wing skin and fuel tank. In such cases, single-sided patch repair is required to restore load-bearing capacity.

Many studies have explored single-sided patch repair for cracked metal panels, evaluating the effects of patch in-plane geometry and other factors on post-repair strength [15–22]. With the increasing prevalence of composite structures, researchers have also studied composite patch repair of CFRP panels, investigating fracture behavior, patch optimization, and adhesive layer design. Sarmah et al. [23] proposed a rapid patch repair method using a co-bonding process based on plasma-induced heating and curing, demonstrating the strength recovery of damaged CFRP. Jiang and Ren [24] precoated the CFRP surface with a CNT-modified resin and reinforced the adhesive layer with aramid pulp micro/nanofibers, improving bending load resistance compared to pure epoxy adhesive. Ji et al. [25] investigated the use of two different adhesives in the longitudinal direction of a single-sided patch repair and observed the bending failure process using acoustic emission and X-ray micro-computed tomography. Li et al. [26] experimentally examined 3D-printed patches in single- and double-sided patch repairs, showing improved tensile strength and stiffness compared to conventional laminated patches. Rashvand et al. [27] restored the stiffness and strength of a damaged unidirectional carbon fiber/polycarbonate coupon using in-situ 3D printing. Kashfuddoja et al. [28] measured strain distribution in the adhesive layer using digital image

* Corresponding author.
E-mail address: yashiro@aero.kyushu-u.ac.jp (S. Yashiro).

https://doi.org/10.1016/j.compstruct.2025.118843
Received 4 July 2024; Received in revised form 15 October 2024; Accepted 2 January 2025
Available online 3 January 2025

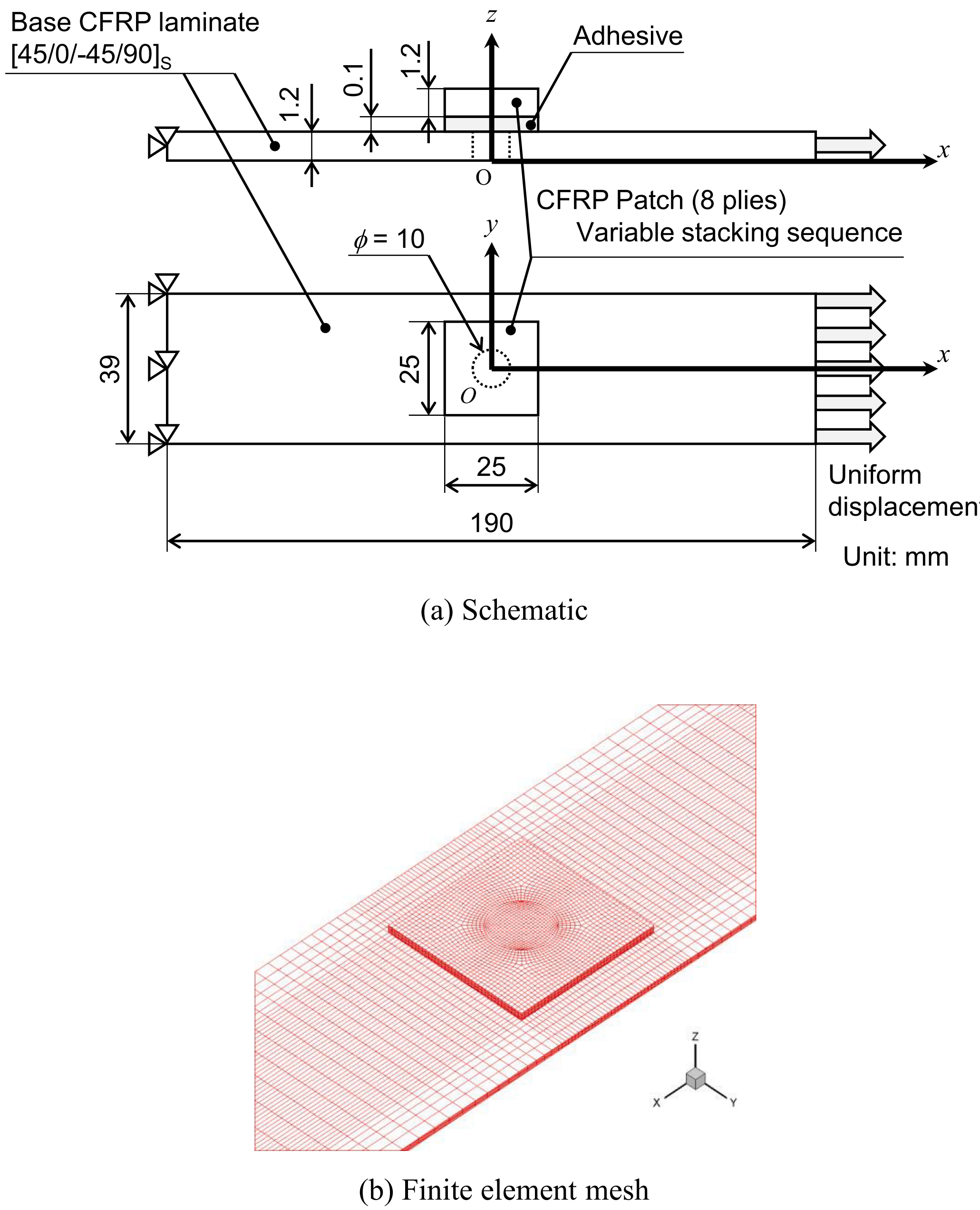

Fig. 1. Numerical representation of a single-sided patch repair for a composite panel.

correlation and observed load transfer from the base plate to the patch near the patch edge, i.e., the shear-lag mechanism. Their observation suggests that tapered patch edges were ineffective in reducing strain in the adhesive layer. Matta et al. [29] experimentally and analytically studied the in-plane compression behavior of open-hole CFRP specimens repaired with CFRP patches on one or both sides. In single-sided repairs, the patch debonded from the patch end, while in double-sided repairs, debonding extended from both the patch end and the hole edge. The repaired specimens ultimately failed after complete patch separation. The recovery of out-of-plane impact resistance properties in single-sided CFRP patch repairs has also been studied [30–33].

A critical issue in patch repair is the low post-repair strength due to patch debonding. In single-sided patch repairs, the neutral plane of bending shifts stepwise through the thickness, causing secondary out-of-plane bending deformation under tensile loading [34,35]. This leads to stress concentration at the patch edge, often resulting in debonding [36,37]. Secondary bending deformation is inevitable in single-sided patch repair, and patch edges are typically tapered to reduce adhesive stress at the patch tip [38].

This study proposes an alternative approach to mitigating patch debonding by utilizing the coupled tensile-bending deformation of asymmetrically stacked CFRP laminates. Based on the classical lamination theory, the relationship between the strain ε^0 and curvature κ of the laminate midplane, the stress resultant N, and the moment per unit length M is described as follows:

$$\begin{Bmatrix} \varepsilon_x^0 \\ \varepsilon_y^0 \\ \gamma_{xy}^0 \\ \kappa_x \\ \kappa_y \\ \kappa_{xy} \end{Bmatrix} = \begin{bmatrix} \alpha_{11} & \alpha_{12} & \alpha_{16} & \beta_{11} & \beta_{12} & \beta_{16} \\ \alpha_{12} & \alpha_{22} & \alpha_{26} & \beta_{21} & \beta_{22} & \beta_{26} \\ \alpha_{16} & \alpha_{26} & \alpha_{66} & \beta_{61} & \beta_{62} & \beta_{66} \\ \beta_{11} & \beta_{21} & \beta_{61} & \delta_{11} & \delta_{12} & \delta_{16} \\ \beta_{12} & \beta_{22} & \beta_{62} & \delta_{12} & \delta_{22} & \delta_{26} \\ \beta_{16} & \beta_{26} & \beta_{66} & \delta_{16} & \delta_{26} & \delta_{66} \end{bmatrix} \begin{Bmatrix} N_x \\ N_y \\ N_{xy} \\ M_x \\ M_y \\ M_{xy} \end{Bmatrix}, \quad (1)$$

Table 1
Material properties used in the analysis.

(a) Base material and patch (CFRP) [40,42–44]	
Longitudinal Young's modulus (GPa)	130
Transverse Young's modulus (GPa)	10
In-plane Poisson's ratio	0.32
Out-of-plane Poisson's ratio	0.49
In-plane shear modulus (GPa)	5.0
Out-of-plane shear modulus (GPa)	3.36
Longitudinal thermal expansion coefficient ($\times 10^{-6}$ K^{-1})	−0.001
Transverse thermal expansion coefficient ($\times 10^{-6}$ K^{-1})	34
(b) Film adhesive [45–47]	
Young's modulus (GPa)	3.0
Poisson's ratio	0.42

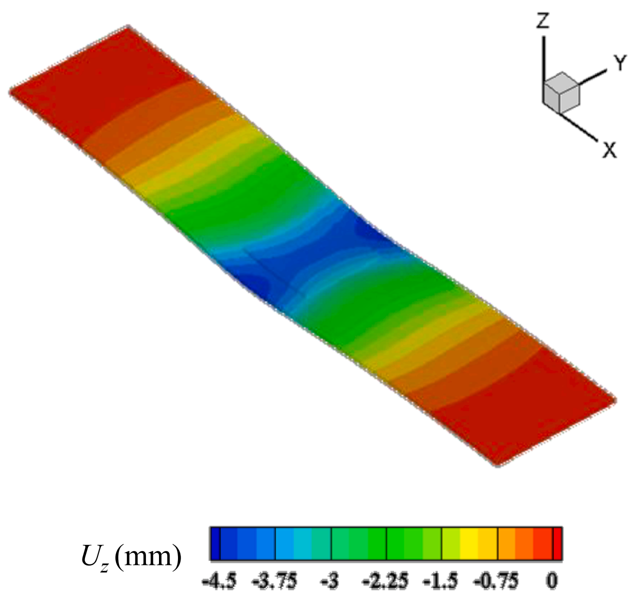

Fig. 2. Out-of-plane deformation of the single-sided patch-repaired CFRP under tensile loading. The stacking sequence of the patch is quasi-isotropic [45/0/-45/90]$_s$.

where α and δ represent the in-plane and bending compliance, respectively, while β denotes the coupling compliance between curvature and in-plane stresses; x and y are the global coordinates in the plane of the laminate. For an asymmetric laminate, in-plane loading generates curvature due to the nonzero β. This study actively utilizes this coupled deformation. Conventional isotropic metals and symmetrically stacked laminates do not exhibit such deformations. The application of these characteristics has traditionally been limited to the aeroelastic tailoring of aircraft wings [39]. Previous research on patch repair has primarily used unidirectional or symmetrically stacked patches. To the best of our knowledge, no studies have been conducted on patches with asymmetric stacking sequences.

This study demonstrates the feasibility of using asymmetrically stacked patches. The stacking sequence of the patch was optimized via a genetic algorithm to achieve a coupled tensile-bending deformation of the patch that is suitable for the secondary bending of the repaired plate, aiming to suppress debonding. Given the innumerable possible stacking sequences for a patch, optimization is essential to achieve the desired stress state in the adhesive layer and to maximize the delay of patch debonding.

The remainder of this paper is organized as follows. Section 2 presents a finite element analysis of a single-sided patch-repaired composite plate subjected to tensile loading and examines the stress state in the adhesive layer. Based on these results, the problem of optimizing the patch's stacking sequence is formulated, and the debonding suppression mechanism is verified by studying the deformation characteristics of the optimal patch. In Section 3, the debonding suppression effect of the asymmetrically stacked patches is experimentally verified. Finally, the findings are summarized in Section 4.

2. Stacking sequence optimization

2.1. Materials and load case scenario

To demonstrate the proposed concept, a simplified geometry and loading scenario was considered in this study, where a quasi-isotropic CFRP laminate with a single-sided patch repair was subjected to uniaxial tensile loading. A standard carbon/epoxy composite (T700SC/#2592, Toray Industries) was used for both the base plate and patch, and a film adhesive (FM300K, Cytec) was employed to bond them. A schematic of the single-sided patch repair on a composite panel is shown in Fig. 1a. The CFRP base plate was 190 mm long and 39 mm wide, consisting of eight stacked plies with a total thickness of 1.2 mm. A 10 mm diameter circular hole was placed at the center of the plate to simulate damage removal. This panel was repaired on one side with a 25 mm square CFRP patch, which also consisted of an eight-ply laminate, similarly 1.2 mm thick. The adhesive layer had a thickness of 0.1 mm. The geometry of the patch-repaired panel was identical to that used in the experiments described in the following section. This study considers a patch-repaired plate subjected to uniaxial tensile loading. One end of the plate was fixed and the other end was subjected to a uniform tensile displacement.

2.2. Finite element analysis

The stress distribution of the single-sided patch-repaired composite plate was predicted using an in-house linear elastic finite element analysis, verified by previous studies [40,41]. The model, as shown in Fig. 1, consisted of a CFRP quasi-isotropic base plate, a CFRP patch, and a thin adhesive layer. The single-sided patch-repaired composite plate was represented by connecting the base material, adhesive, and patch with high-stiffness spring elements. The materials used were standard CFRP and structural film adhesives, with their properties listed in Table 1.

The base material had a stacking sequence of [45/0/-45/90]$_s$, with a circular hole in the center simulating the damage removal region. Based on classical lamination theory [48], the homogenized Young's modulus and shear modulus were 56.2 GPa and 19.3 GPa, respectively, and the bending stiffness D_{11} was 13.0 N·m, where direction 1 coincides with the longitudinal axis of the base plate. The patch had a variable stacking sequence with eight plies. Three-dimensional, eight-node hexahedral solid elements were employed, comprising 58,880 elements and 70,213 nodes. A detailed formulation of the finite element analysis and isoparametric elements used can be found in the literature [49]. Due to the high computational cost of the optimization process, the base material and patch were modeled with one element per ply in the through-thickness direction. One end of the base plate was fixed in the longitudinal direction, while a uniform tensile displacement of 2.09 mm (corresponding to a 1.1 % strain) was applied to the opposite end. In this study, the stacking sequence of the patch was optimized both with and without consideration of thermal deformation during manufacturing, assuming a temperature change ΔT of − 110 °C.

Fig. 2 shows the out-of-plane displacement distribution when using a quasi-isotropic patch. Tensile loading induced a convex downward deformation in the z-direction, referred to as secondary bending. This type of deformation was confirmed through preliminary experiments using stereo digital image correlation.

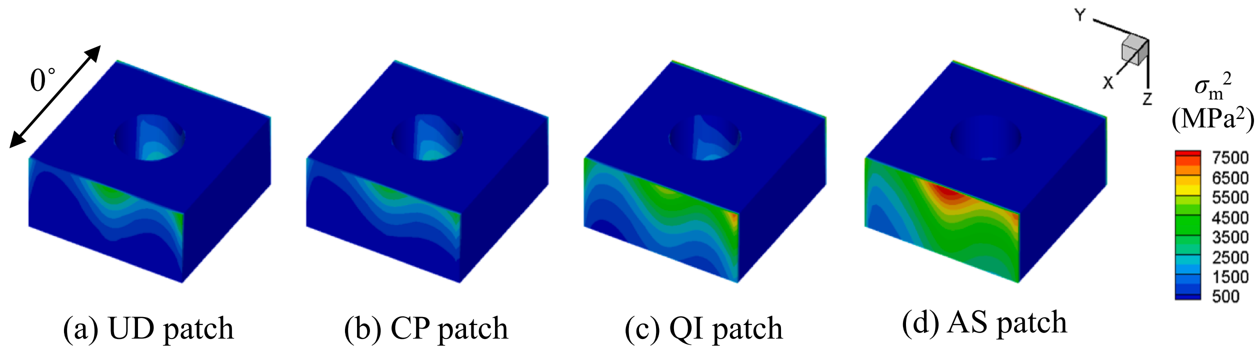

Fig. 3. Comparison of the squared hydrostatic stress distribution in the adhesive (z-direction magnified by 125). The bottom of the figure shows the surface in contact with the patch.

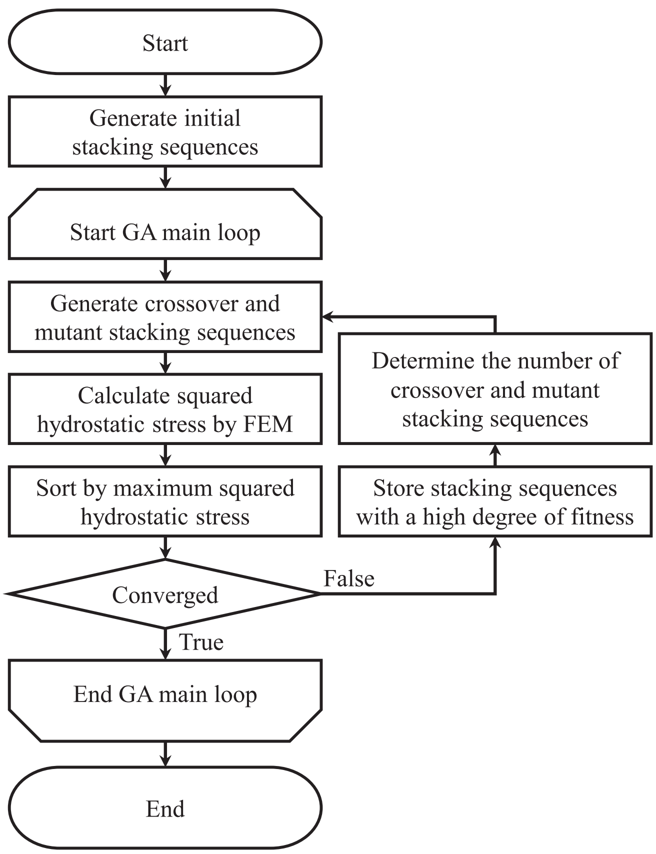

Fig. 4. Flowchart illustrating the genetic algorithm used to optimize the stacking sequence of the patch.

2.3. Stress analysis

Patch debonding can be regarded as damage to the adhesive resin. When hydrostatic stress increases in a polymeric material, a critical state called microcavitation is reached owing to volume expansion. Asp et al. [50] considered this as the main cause of resin cohesive failure and proposed a failure criterion based on the expansion strain energy density U_v as follows:

$$U_v \approx \frac{1}{2}\sigma_m\varepsilon_v = \frac{3(1-2\nu)}{2E}{\sigma_m}^2 \geq U_v^c, \tag{2}$$

where σ_m represents the hydrostatic stress, ε_v is the volumetric strain, E and ν are Young's modulus and Poisson's ratio, respectively, and U_v^c is the critical value of U_v at failure. Equation (2) suggests that adhesive damage occurs when the square of the hydrostatic stress reaches a critical threshold at a given point in the adhesive.

In practice, the axial stiffness of the patch is typically matched to that of the base laminate to preserve the original in-plane load path. However, this study focuses exclusively on patch debonding and permits different stacking sequences in both the base laminate and the patch. Stress analysis was conducted on four basic stacking sequences for patches: unidirectional $[0_8]$ (referred to as UD), cross-ply $[0_2/90_2]_S$ (CP), quasi-isotropic $[45/0/\text{-}45/90]_S$ (QI), and asymmetric cross-ply $[0_4/90_4]$ (AS). Secondary bending, as shown in Fig. 2, occurred consistently across all patch types, but the magnitude of the out-of-plane deformation varied with the stacking sequence. The maximum displacement was recorded as 3.71 mm for the UD patch, 4.09 mm for the CP patch, 4.46 mm for the QI patch, and 4.14 mm for the AS patch. These variations in out-of-plane deformation are attributable to differences in the bending stiffness D_{11}, which relates to the moment M_x and curvature κ_x. The bending stiffness D_{11} was 18.7, 16.7, 9.8, and 10.2 N·m for the UD, CP, QI, and AS patches, respectively. A higher D_{11} value corresponds to less secondary bending deformation.

Fig. 3 illustrates the distribution of ${\sigma_m}^2$ within the adhesive layer, magnified 125 times in the through-thickness direction for enhanced clarity. The hydrostatic stress was observed to be concentrated at the longitudinal edge of the adhesive, where debonding initiated during preliminary experiment. Therefore, the square of the hydrostatic stress was found to be an appropriate measure for determining susceptibility to debonding. In the UD and CP patches, ${\sigma_m}^2$ was smaller compared to the QI patch, as the higher bending stiffness in the UD and CP patches resulted in smaller out-of-plane displacement. This, in turn, caused the adhesive to be pinched at the patch edges during secondary bending, leading to pseudo-compression. However, despite the smaller out-of-plane displacement in the AS patch compared to the QI patch, the AS patch generated larger ${\sigma_m}^2$ values locally. This indicates that the patch's bending deformation significantly influences the stress distribution within the adhesive layer, suggesting that merely reducing secondary bending deformation may not be sufficient for controlling patch debonding.

2.4. Problem setup

The stacking sequence of the patch was optimized to suppress debonding based on a genetic algorithm (GA) using the stress analysis described in the previous section. The optimization problem for the stacking sequence of a patch is defined as follows:

$$\begin{aligned} &\text{Design variable } \theta_i = n_i \times \Delta\theta \ (i = 1, \cdots, 8) \\ &\text{Minimize } {\sigma_{m,\text{Max}}}^2 \end{aligned} \tag{3}$$

where the design variable θ_i ($-90^\circ < \theta_i \leq 90^\circ$) represents the fiber orientation angle for the eight patch plies. The value of θ_i is discretized into integer multiples n_i of a fiber orientation angle interval $\Delta\theta$. Three

Table 2
Optimal stacking sequence for the composite patch, with the first ply positioned on the free surface side.

(a) Without temperature change

$\Delta\theta$	Stacking sequence	$\sigma^2_{m,\mathrm{Max}}$ (MPa^2)	β_{11} (N^{-1})	D_{11} (N·m)
5°	[0/20/−80/−85/−85/−85/15/5]	3254.2	1.08×10^{-3}	15.7
15°	[0/15/−75/90/90/30/0/0]	3356.4	2.03×10^{-3}	16.9
45°	[0/0/90/90/90/45/0/0]	3433.9	6.51×10^{-4}	16.9

(b) With temperature change ($\Delta T = -110$ °C)

$\Delta\theta$	Stacking sequence	$\sigma^2_{m,\mathrm{Max}}$ (MPa^2)	β_{11} (N^{-1})	D_{11} (N·m)
5°	[0/0/−65/70/65/5/30/−25]	3175.1	-4.34×10^{-3}	15.0
15°	[0/0/−75/−60/−60/0/30/−15]	3300.8	-1.95×10^{-3}	15.9
45°	[0/0/0/90/90/0/−45/0]	4036.0	-3.60×10^{-3}	16.7

different $\Delta\theta$ values were used: 5°, 15°, and 45°. The objective function is the highest square of the hydrostatic stress among all adhesive elements. Because σ_m is always positive in the analysis setup described in the previous section, its sign was not considered in the objective function.

An in-house GA code was used for the optimization. In actual manufacturing, laminates with orientation angles that are integer multiples of $\Delta\theta$ are typically used. The GA is particularly suitable for optimization using these discrete values. The details of the GA are described in the Appendix. A flowchart illustrating the optimization process is shown in Fig. 4. Stacking sequences for eight patch plies were generated as initial individuals according to $\Delta\theta$, with the total number of individuals determined in advance. Crossovers and mutations were generated from these stacking sequences by considering the fiber orientation angle of each ply as a gene. The numbers of crossovers and mutations were set to 0.5 and 0.6 times the total number of individuals, respectively. The number of mutations was adjusted to increase and the number of crossovers was adjusted to decrease in subsequent generations to avoid duplication in individuals. Among the generated crossovers, mutations, and initial individuals in a generation, as many individuals with a small objective function were retained as the total number of individuals and were used as initial individuals for the next generation. This process was repeated until convergence was achieved. Individuals generated once but not used in the subsequent generation were prohibited from appearing as mutant individuals. In this study, the total number of individuals was set to 120 when $\Delta\theta = 5°$, 70 when $\Delta\theta = 15°$, and 50 when $\Delta\theta = 45°$. The maximum number of generations was 150, and the optimization was considered to converge when the number of different stacking sequences was less than or equal to two, and the best stacking sequence did not change over 15 generations.

2.5. Optimization results

Table 2 presents the optimal stacking sequences, all of which are asymmetric. Plies oriented near 0° were positioned at the top and bottom of the patch, while those near 90° were clustered slightly above the center of the laminate thickness. In the absence of temperature change, all of these stacking sequences exhibited positive coupling compliance β_{11}, which represents the coupling between the load N_x and curvature κ_x in the longitudinal direction, as described by classical lamination theory.

Fig. 5 illustrates the distribution of the square of the hydrostatic stress in the adhesive with the optimized patches. Compared to the QI patch case (Fig. 3c), the square of the hydrostatic stress at the patch edge, where debonding was likely to occur, decreased after optimizing the stacking sequence. The stress distribution in the adhesive is shown in Fig. 6, where the near-0° plies on the free surface side of the optimal patch contributed to an increase in the bending stiffness D_{11}. Similar to the UD and CP patches, the difference in D_{11} between the optimal patch

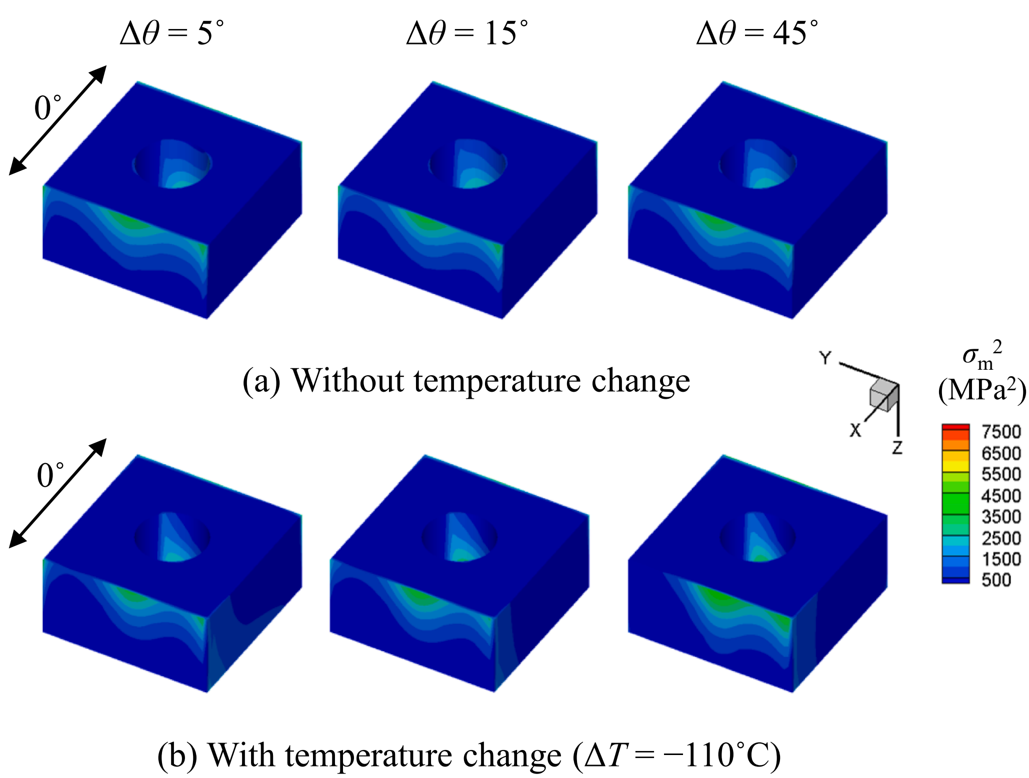

Fig. 5. Squared hydrostatic stress distribution in the adhesive achieved by the optimal patches (z-direction magnified by 125).

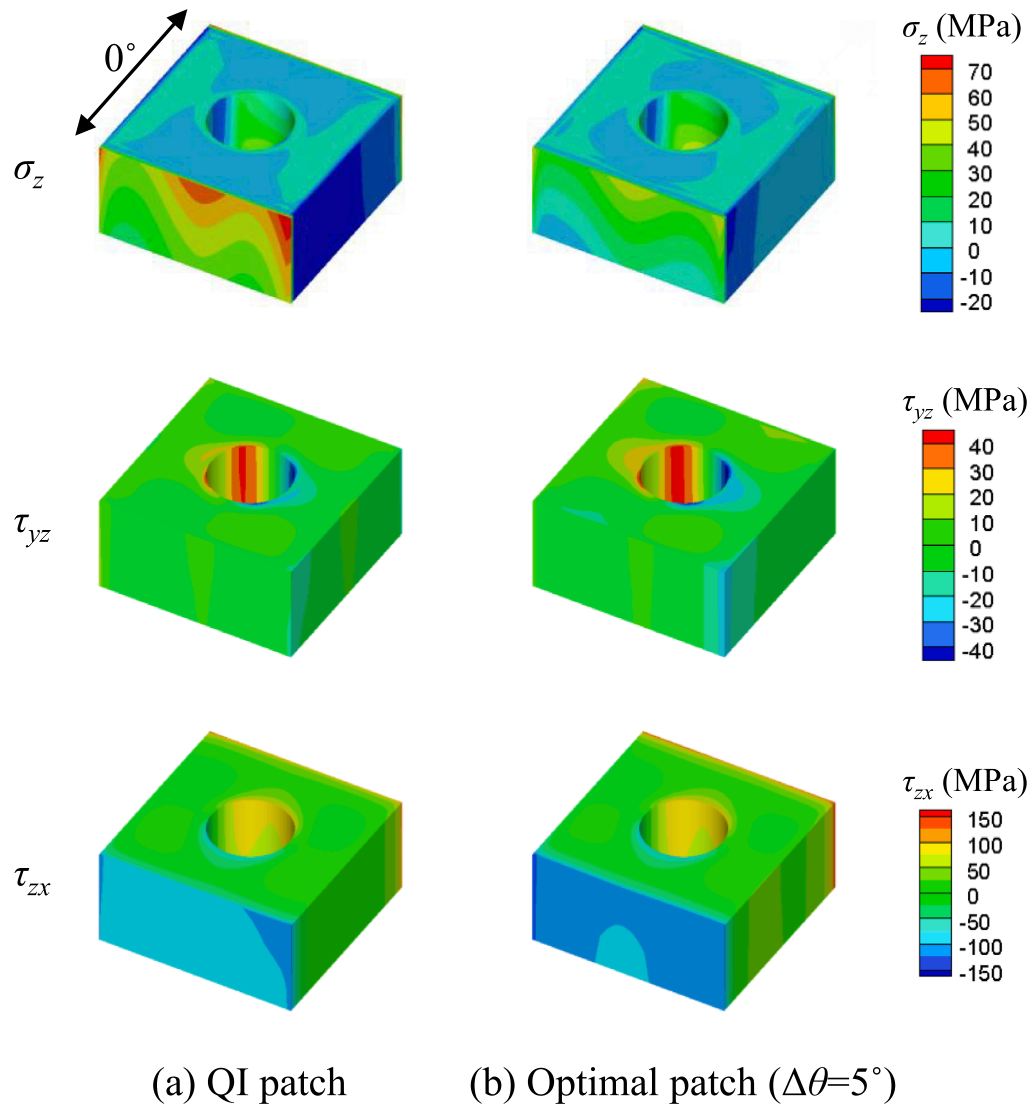

Fig. 6. Stress distribution in the adhesive without considering temperature changes (z-direction magnified by 125).

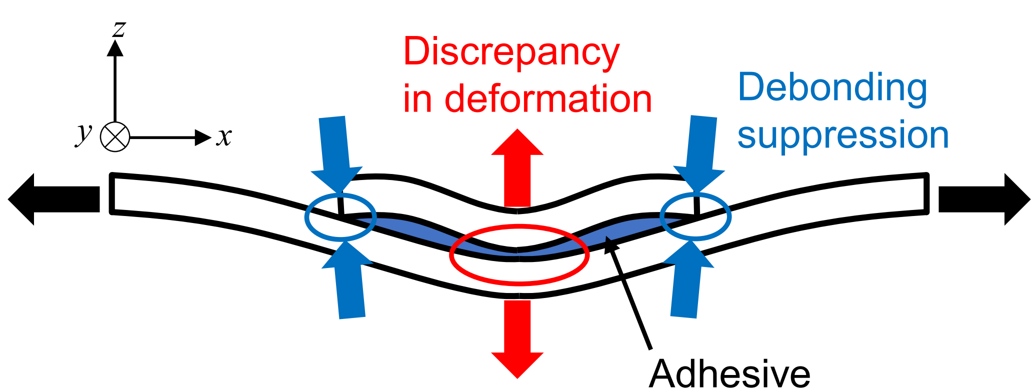

Fig. 7. Mechanism of Mode I peeling suppression facilitated by the optimal patch.

and the base QI laminate helped alleviate peel stress σ_z, reducing the contribution of Mode I in patch debonding. The shear stress distribution varied slightly depending on the patch type.

The positive coupling compliance β_{11} leads to a bending deformation of the optimal patch, producing an upward convex curvature under tensile loading. Fig. 7 provides a schematic of the debonding suppression mechanism in the asymmetrically stacked patch repair. When a tensile load is applied and the patch elongates, the patch itself deforms in an

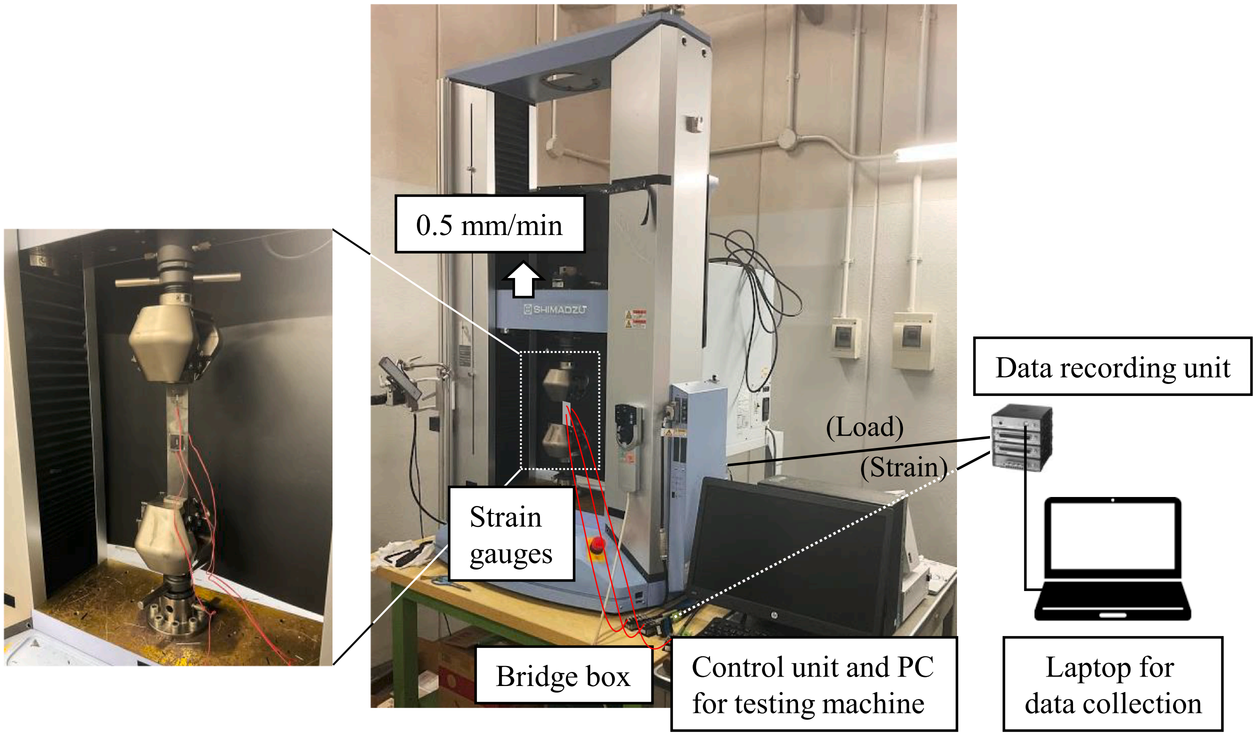

Fig. 8. Schematic diagram of the experimental setup.

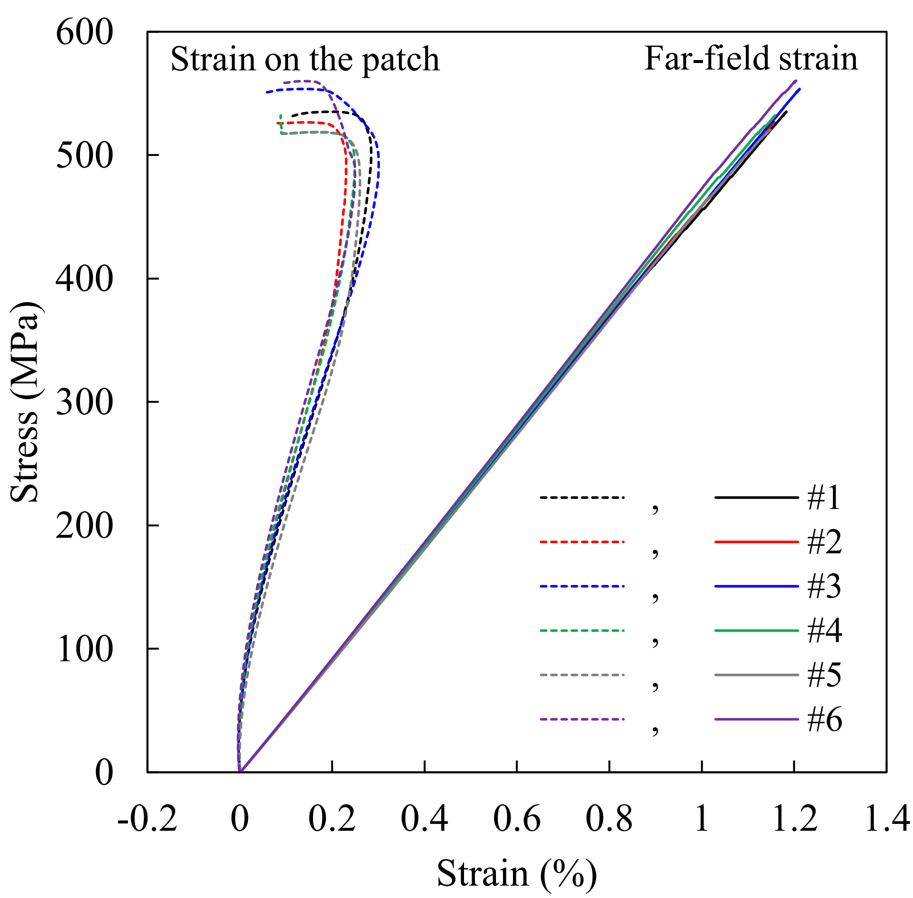

Fig. 9. Stress–strain curves for the specimen repaired with QI patch.

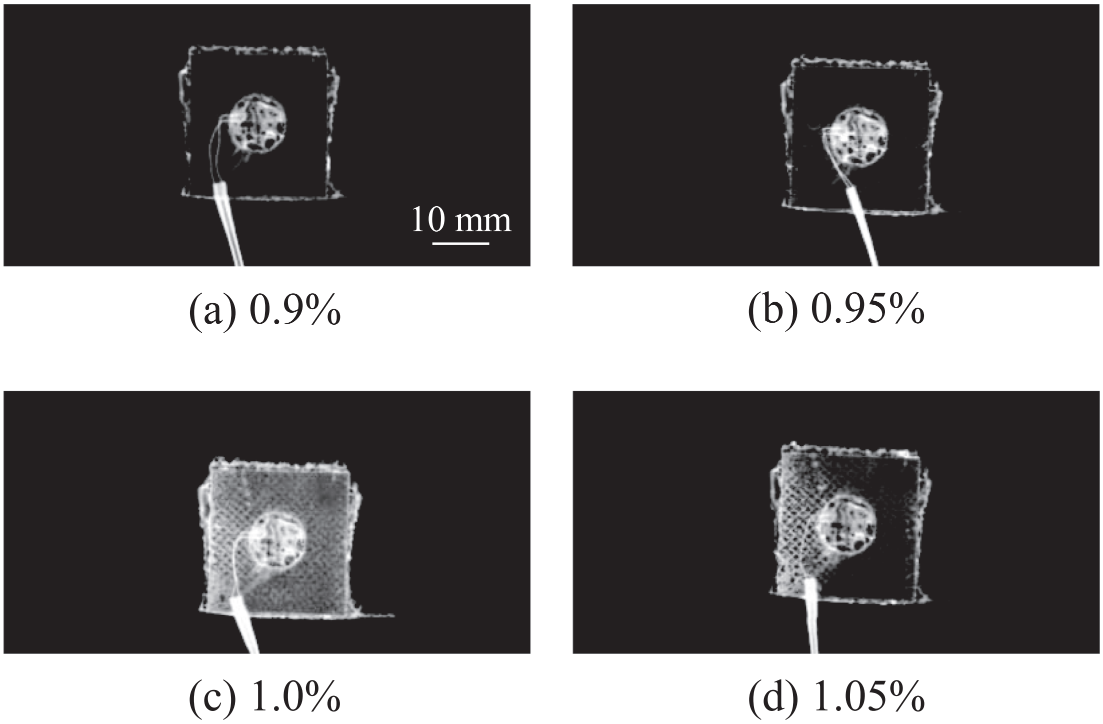

Fig. 10. Soft X-ray image illustrating the progress of debonding in a patch-repaired composite specimen, featuring a QI patch adhered to one side of the coupon.

Table 3
Comparison of debonding onset strain and strength between QI and optimal patches.

	QI patch		Opt patch		OptT patch	
	Debonding onset strain (%)	Strength (MPa)	Debonding onset strain (%)	Strength (MPa)	Debonding onset strain (%)	Strength (MPa)
#1	1.109	535.2	1.111	567.3	1.010	536.0
#2	1.078	526.8	1.097	536.1	0.992	535.0
#3	1.075	553.6	1.082	537.9	0.960	519.0
#4	1.059	532.1	1.024	522.2	0.950	509.4
#5	1.051	520.6	1.024	521.4	0.900	488.1
#6	1.022	560.2	–	–	–	–
Average	1.066	538.1	1.068	537.0	0.962	517.5
Standard deviation	0.027	14.2	0.037	16.6	0.038	17.8
Correlation coefficient	−0.350		0.860		0.987	

upward convex manner due to the tensile-bending coupling effect. However, the entire repaired plate exhibits downward convex deformation as a result of secondary bending. This discrepancy between the patch and plate deformations alleviates Mode I deformation at the patch edge and reduces positive peel stress. Consequently, hydrostatic stress is mitigated, and adhesive damage is suppressed.

In the presence of temperature changes, 0° plies were placed on the free surface side, plies near ± 30° were positioned on the adhesive side, and plies around ± 65° were located slightly on the free surface side of the midplane (Table 2). These patches deformed convexly upward due to thermal residual stress. However, because the coupling compliance β_{11} is negative in these stacking sequences, the tensile load produces a downward convex deformation. The upward convex thermal residual deformation is greater than the downward convex deformation caused by tensile-bending coupling, resulting in the same debonding suppression mechanism illustrated in Fig. 7.

3. Experiment

The patch with the optimal stacking sequence, determined at $\Delta\theta = 5°$ without temperature change, is referred to as the 'Opt' patch, and that in the presence of temperature change is referred to as the 'OptT' patch. Tensile tests were conducted on single-sided patch-repaired composite plates to demonstrate the effectiveness of these optimal patches in suppressing debonding.

3.1. Materials and procedure

The dimensions of the specimen were identical to those of the model (Fig. 1) but extended by 60 mm longitudinally for gripping purposes. The base plate measured 250 mm in length and 39 mm in width, with a patch measuring 25 mm square. The specimen consisted of a CFRP quasi-isotropic base plate with a 10 mm diameter open hole, a CFRP patch, and a film adhesive. The patch was adhered to the center of the base laminate using a film adhesive. The QI, Opt, and OptT patches were used for repair. The stacking sequence of the base laminate and QI patch was $[45/0/\text{-}45/90]_s$, while the Opt and OptT patches had stacking sequences of $[0/20/\text{-}80/\text{-}85_3/15/5]$ and $[0_2/\text{-}65/70/65/5/30/\text{-}25]$, respectively. A carbon/epoxy composite (T700SC/#2592, Toray) was used for both the base material and patches, and Cytec FM300K film adhesive was employed. The volume fraction and glass transition temperature of the CFRP were 60 % [51] and 92 °C [52], respectively. The base laminates and patches were cured in an autoclave at 130 °C and 0.3 MPa for 1 h, then cut to the required dimensions. The bonding surfaces

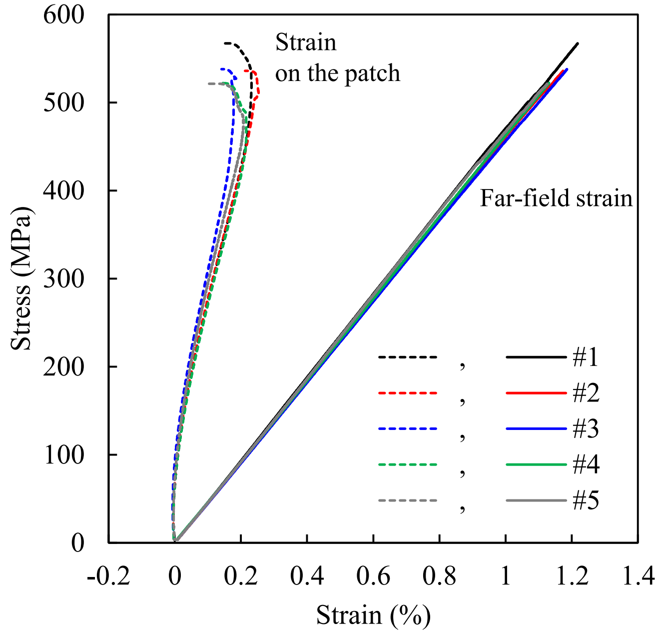

(a) Opt patch

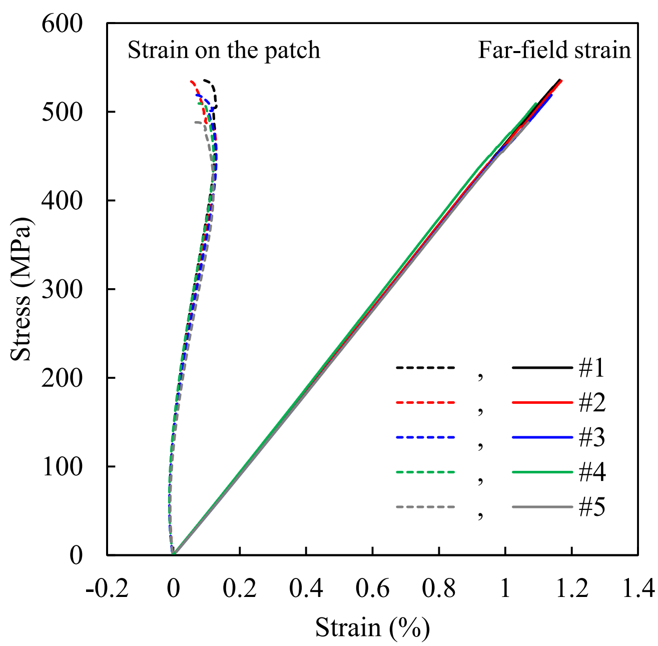

(b) OptT patch

Fig. 11. Stress–strain curves of the specimen repaired with (a) Opt or (b) OptT patch.

were sanded, wiped with acetone, and adhered using film adhesive in an autoclave at 175 °C and 0.1 MPa for 1 h. The fracture properties of the film adhesive are documented in the literature [47,53].

Six specimens were prepared for the QI patch, and five for both the Opt and OptT patches. After the patches were adhered, strain gauges (with a gauge length of 5 mm and resistance of 120 Ω) were attached to the center of the patch and on both sides of the central axis of the base laminate, away from the circular hole. Fig. 8 provides a schematic of the experimental setup. Both ends of the specimen (30 mm) were clamped using a sand cloth. Tensile tests were performed at room temperature at a crosshead speed of 0.5 mm/min until fracture using an electromechanical universal testing machine (AG-50kNXDplus, Shimadzu). The load and strains were measured simultaneously during the test.

3.2. Results and discussion

Fig. 9 presents the stress–strain curves of the patch-repaired composite plate using the QI patch. The stress, shown on the vertical axis, represents the load divided by the initial cross-sectional area of the base plate away from the patch. The strain, on the horizontal axis, reflects the value from the strain gauge at the center of the patch or the average from gauges placed on the front and back surfaces at a distance from the hole. The relationship between stress and far-field strain remained linear, while the strain on the patch increased nonlinearly with the applied stress due to secondary bending. Soft X-ray radiography of an additional QI patch specimen (Fig. 10) captured the progression of patch debonding. The specimen was unloaded at intervals of 0.05 % applied strain, a contrast agent was applied around the patch, and the specimen was reloaded after each observation. Audible noise occurred during loading after observation at 0.95 % strain, and patch debonding spread to the left half of the adhesive. This observation suggests a rapid progression of patch debonding. As the debonding reached the center of the patch, the repair effectiveness was nearly lost, leading to a decrease in patch strain despite increased tensile load. Specimen QI-#4 failed after the patch strain remained constant despite increasing load, and specimens QI-#2, #5, and #6 fractured immediately after the patch strain ceased to vary. The average strength of the QI-patch specimens was 538.1 MPa (Table 3). The tensile strength of the open-hole base plate without a patch was 506 MPa, whereas the pristine QI laminate had a strength of 945 MPa. The single-sided repair provided only minimal strength recovery. These observations indicate that failure occurred once the QI patch debonding reached the center and stopped progressing.

Fig. 11 illustrates the stress–strain curves of the specimens with Opt and OptT patches. The far-field curves exhibited the same stiffness as those with the QI patch, regardless of the patch type. Even with the optimal patch, unloading resulted in a reduction in strain at the center of the patch. However, the reduction in strain for the Opt and OptT patches was smaller than for the QI patch, with some specimens (Opt-#2 and #3, and OptT-#1 and #3) displaying a sudden, slight increase in strain. This difference suggests that debonding behavior varies with the patch type.

When a repaired specimen breaks after complete patch separation, the strength is dependent on the base plate's strength (i.e., the state of open-hole processing) and the stress concentration caused by the relative position of the open hole and the debonding tip. Table 3 lists the strength values for each specimen, and a one-way analysis of variance (ANOVA) was performed to assess whether the difference between the means of the three patch types was statistically significant. The significance level was set at 0.05; a p-value below this threshold indicates that the null hypothesis can be rejected with 95 % confidence. The equality of the variances of the two populations was tested using the F statistic, which follows an F distribution. The strength results showed no statistically significant difference between the test groups ($F(2,13) = 2.166$, where the two arguments of F are the degrees of freedom between and within the groups, respectively; $p = 0.154$). Therefore, strength comparisons are not suitable for investigating the effect of stacking sequence optimization on debonding suppression.

The far-field strain at which the strain on the patch reached its maximum was defined as the debonding onset strain. Table 3 provides the debonding onset strains of each specimen and their averages. A one-way ANOVA revealed a statistically significant difference in debonding onset strain between the test groups ($F(2,13) = 13.29$, $p = 0.000719 < 0.05$), indicating that the patch type influences the onset of debonding. In the QI patch, a slightly negative correlation was observed between debonding onset strain and strength, suggesting that the repair

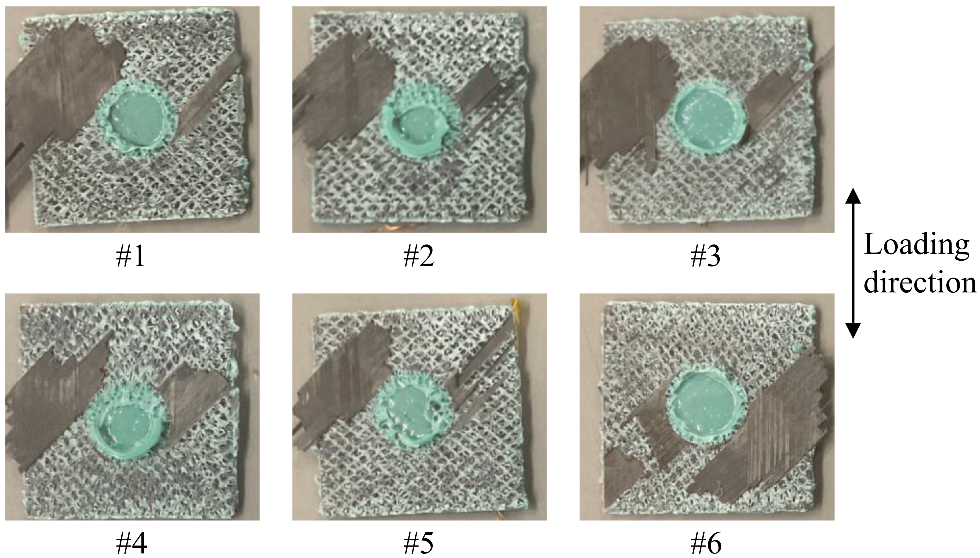

Fig. 12. Overview of the separated surface of the QI patch.

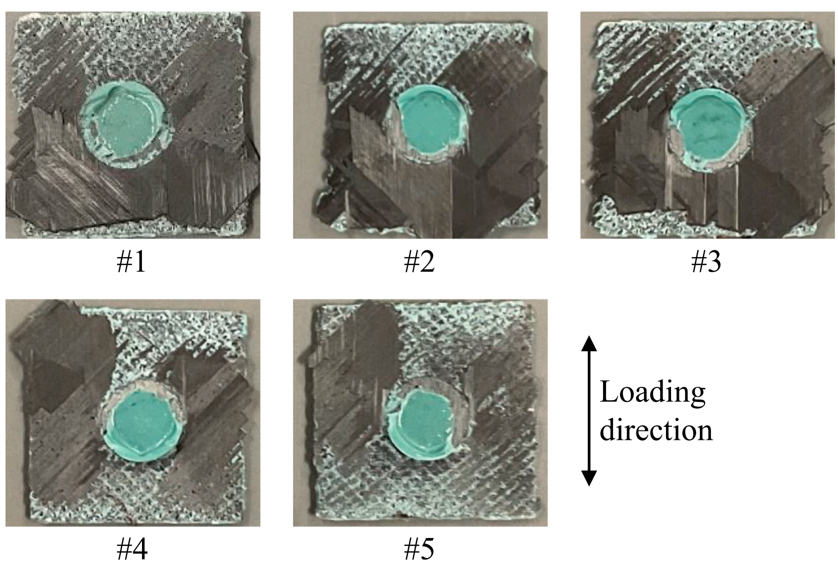

Fig. 13. Overview of the separated surface of the Opt patch.

effectiveness diminished before final failure. The average debonding onset strain for the Opt patch was similar to that for the QI patch; however, the Opt patch results were divided into two groups: a higher group (specimens #1, #2, and #3) of approximately 1.1 % and a lower group (specimens #4 and #5) of approximately 1.02 %. A positive correlation was observed between debonding onset strain and strength in the Opt patch, indicating that the debonding process influenced strength, unlike in the QI patch.

Figs. 12 and 13 provide an overview of the separate QI and Opt patches after testing. Most of the QI patch surface was covered with adhesive, indicating cohesive failure. In contrast, material failure was observed on the Opt patch, with CFRP from the base plate remaining attached. This transition from cohesive failure to base plate delamination is also suggested by the sudden increase in the patch strain seen in Fig. 11. With the Opt patch, the specimen failed as soon as the strain on the patch began to decrease due to delamination, compromising the integrity of the base plate. Thus, the Opt patch demonstrated a clear relationship between debonding onset strain and strength. In specimens Opt-#1, #2, and #3, coupled tensile-bending deformation functionally suppressed patch peeling, leading to material failure of the adhesive at the edges, which had relatively higher strength. However, the adhesive remaining on specimens Opt-#4 and #5 was larger than in specimens #1–#3. Differences in the debonding or delamination crack growth interface affected the difficulty of patch debonding, likely due to the challenge of bonding patches with warping deformation caused by thermal residual stresses.

The debonding onset strain of the OptT patch was significantly lower than that of the QI patch (Table 3). The OptT patch's higher thermal residual stresses caused greater warping deformation than in the Opt patch, making homogeneous adhesion difficult. Ideally, warping deformation should suppress peel stress and delay debonding, as shown in Fig. 7. However, once debonding started, the free edge of the patch was pressed against the base plate by residual warping, increasing the peel stress at the debonding crack tip. As with the Opt patch, cohesive failure transitioned to base plate delamination, leaving CFRP plies on the separated OptT patches. These mechanisms explain the lower debonding onset strain and strength of the OptT patch.

This study examined patch debonding in a single-sided patch-repaired composite plate under simple uniaxial tensile loading. Applying this asymmetrically stacked patch approach to more complex

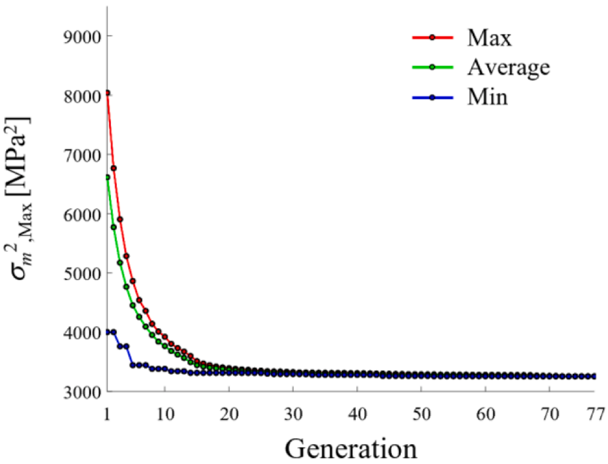

(a) Without temperature change

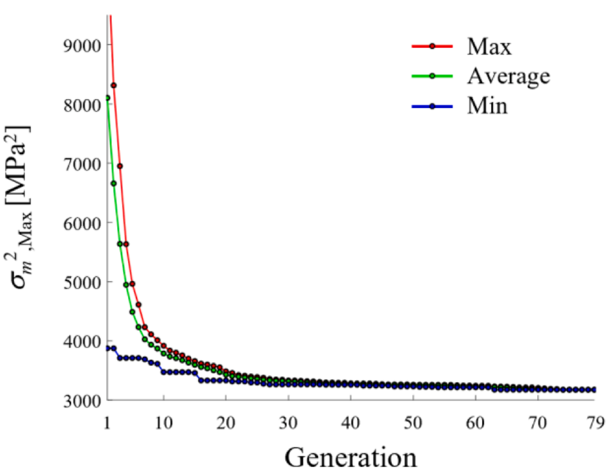

(b) With temperature change ($\Delta T = -110^\circ$C)

Fig. 14. History of the maximum squared hydrostatic stress during the optimization of the stacking sequence ($\Delta\theta = 5^\circ$).

loading scenarios (e.g., biaxial loading) will be a focus of future work. By incorporating the geometry and loading conditions into the finite element model, an optimal stacking sequence for each loading scenario can be determined. One limitation of this study is its exclusive focus on patch debonding. In practical applications, acceptable in-plane stiffness ranges, considering the in-plane load path, should be incorporated as constraints in stacking sequence optimization.

The repair efficiency (i.e., the ratio of the post-repair strength to the pristine laminate strength) with the Opt patch was 57 %, which was lower than that with scarf repair (64–80 % depending on the repair design [54]), because secondary bending is unavoidable as long as the patch is attached to one side. To implement this approach in in-situ repairs, several points should be addressed from an analytical perspective. The loading conditions at the repair site must be identified and appropriately applied to the finite element model as boundary conditions. Not only the stacking sequence but also the size of the patch must be optimized to provide sufficient load-bearing capacity with minimal increase in weight. However, the computational cost of optimization with many design variables is high. To reduce this, an efficient analysis model and optimization algorithm are needed.

4. Conclusions

This study proposed an effective repair concept for composite structures by leveraging the coupled tensile-bending deformation of an asymmetrically stacked laminate, which helps suppress patch debonding caused by secondary bending deformation in single-sided patch repairs. The stacking sequence, or fiber orientation angle of the plies in the patch, was optimized using a GA to minimize the square of the hydrostatic stress in the adhesive layer securing the patch to the quasi-isotropic base laminate.

The optimal asymmetrically stacked patch induced bending deformation opposite to the secondary bending due to tensile-bending coupling compliance. This bending discrepancy alleviated the expansion strain energy density in the adhesive at the longitudinal edge, reducing the Mode I contribution to patch debonding. By accounting for temperature changes, a stacking sequence was identified where thermal residual warping pushed the patch edges against the base plate, thereby reducing peel stress.

The mechanism for patch-debonding suppression through the optimized asymmetric stacking sequence was experimentally validated. Tensile tests on single-sided patch-repaired CFRP plates showed that cohesive failure of the adhesive occurred with the QI patch, with the specimen failing after the patch lost its load-bearing capacity. In contrast, with the Opt patch, cohesive failure of the adhesive transitioned to delamination in the base CFRP plate, resulting in material failure that caused final failure before the patch was fully unloaded. The results for the Opt patch were divided into two groups: one with a larger area of material failure and the other with a smaller area. The debonding onset strain and strength of the first group were equal to or greater than those of the QI patch.

In the Opt patch, delamination of the base plate likely deteriorated its integrity and accelerated final failure. To further enhance the effectiveness of single-sided patch repair, optimization of the patch stacking sequence, considering the fiber orientation at the bonding surface of the base plate (which influences the transition from cohesive failure to delamination), is necessary.

CRediT authorship contribution statement

Kohei Hashimoto: Writing – original draft, Visualization, Software, Methodology, Investigation, Formal analysis, Data curation. **Shigeki Yashiro:** Writing – review & editing, Validation, Supervision, Resources, Project administration, Methodology, Conceptualization. **Sota Onodera:** Writing – review & editing, Validation, Formal analysis. **Kazuki Ryuzono:** Writing – review & editing, Validation, Software.

Declaration of competing interest

The authors declare that they have no known competing financial interests or personal relationships that could have appeared to influence the work reported in this paper.

Acknowledgement

A part of this work was supported by JSPS KAKENHI Grant Number 23K26299.

Appendix. Genetic algorithm

The stacking sequence of the patches was optimized to create patches that are less likely to debond during CFRP single-sided patch repairs. Specifically, the genetic algorithm (GA) was employed to vary the fiber orientation angles of the eight plies in the patch as genes, aiming to minimize the maximum value of the square of the hydrostatic stress in the adhesive elements, $\sigma_{m,\mathrm{Max}}^2$. The GA is inspired by biological evolution principles, such as selective crossover and mutation, and serves as a method for stochastic search, learning, and optimization. Crossover and mutation individuals are generated from a population of stacking sequences (i.e., generation), and individuals are selected in ascending order of fitness (or objective function) to form the next generation's population. Individuals with superior gene expression remain even after this process is repeated. In selective crossover, two individuals are chosen from the population to serve as parents, generating two offspring from their genes. Chromosomes of the offspring are formed by inheriting genes from the same locus (i.e., the index of a ply) of one parent and taking genes from different parents in the offspring. The appropriate selection of superior individuals as parents produces crossover individuals with advantageous genes. These superior genes are then disseminated throughout the population, facilitating the identification of strong individuals. Mutation, an operation that randomly alters a portion of a chromosome's value, allows exploration of alternatives beyond the initial combination of genes. However, excessive mutant individuals can lead to a random search, slowing convergence.

The stacking sequence optimization problem is defined in Eq. (3), where the GA takes an integer multiple n_i of the fiber orientation angle interval $\Delta\theta$ as a gene. A flowchart of the optimization process, presented in Fig. 2, is described in detail.

– Generate initial stacking sequences: A defined number of initial individuals are randomly generated, and $\sigma_{m,\mathrm{Max}}^2$ values of these individuals are calculated through stress analysis.

– Generate crossover and mutant stacking sequences: A predetermined number of crossover and mutant individuals are produced. To generate crossover individuals, the required number of parental individuals is randomly selected from the population. The stacking sequences of the parents are crossed using the uniform crossover method to create two offspring. The mask utilized in the uniform crossover method is a random sequence of zeros or ones corresponding to the ply index's chromosome lengths. For the generation of mutant individuals, a predetermined number of mutant mothers are selected from the population, with a specified number of n_i $(i = 1, \ldots, 8)$ randomly altered. If the generated mutant matches the lower-fitness individuals of previous generations, it is canceled, and the mutation process is repeated.

– Calculate squared hydrostatic stress by FEM: Finite element analysis is conducted to calculate $\sigma_{m,\mathrm{Max}}^2$ for the newly generated crossover and mutant individuals. For individuals remaining from the previous generation, previously calculated values are used.

– Sort by maximum squared hydrostatic stress: The initial, crossover, and mutant individuals are sorted in order of decreasing $\sigma_{m,\mathrm{Max}}^2$ as better-fitted individuals.

– Store stacking sequences with a high degree of fitness: A predetermined number of individuals with higher fitness levels are retained as the population for the next generation. Individuals with lower fitness levels are stored in a library to prevent their emergence as mutant individuals in subsequent generations.

– Determine the number of crossover and mutant stacking sequences: When the number of stacking sequences in a population (i.e., diversity) is small, generating new individuals through crossover becomes difficult due to multiple individuals with the same chromosome in that generation. In such cases, new stacking sequences can be explored by reducing the number of crossovers and increasing the number of mutants. Consequently, the ratio of crossover and mutant individuals to the predetermined number of individuals in a generation is adjusted based on diversity.

– Convergence judgment: Convergence is assumed to have been achieved when all of the following conditions are satisfied: (1) diversity is less than three, (2) the minimum value of $\sigma_{m,\mathrm{Max}}^2$ has not been updated for 15 generations, and (3) no new mutant individuals can be generated for five generations by matching less-fit individuals in the library.

Several parameters in the GA govern each operation: the number of individuals in a generation, the maximum number of generations, the ratio of the number of crossovers (mutants) to the number of individuals in a generation, and the ratio of the number of genes to be mutated to the total number of genes in an individual. By varying these parameters, the speed required to reach convergence and the ability to avoid local optimal solutions can be adjusted. However, there are no established guidelines for determining these parameters for general problems, necessitating their determination for each specific optimization challenge.

Fig. 14 illustrates the history of the maximum, minimum, and average values of $\sigma_{m,\mathrm{Max}}^2$ over the generations during the stacking sequence optimization defined in Section 2.2. The values of $\sigma_{m,\mathrm{Max}}^2$ decreased monotonically and converged to a constant value over generations, both with and without temperature change. In all instances, the optimization converged before reaching the maximum number of generations. The optimal stacking sequences are listed in Table 2.

Data availability

Data will be made available on request.

References

[1] Mohammadi S, Yousefi M, Khazaei M. A review on composite patch repairs and the most important parameters affecting its efficiency and durability. J Reinf Plast Compos 2021;40:3–15. https://doi.org/10.1177/0731684420941602.
[2] Psarras S, Loutas T, Galanopoulos G, Karamadoukis G, Sotiriadis G, Kostopoulos V. Evaluating experimentally and numerically different scarf-repair methodologies of composite structures. Int J Adhes Adhes 2020;97:102495. https://doi.org/10.1016/j.ijadhadh.2019.102495.
[3] Katnam KB, Da Silva LFM, Young TM. Bonded repair of composite aircraft structures: A review of scientific challenges and opportunities. Prog Aeros Sci 2013;61:26–42. https://doi.org/10.1016/j.paerosci.2013.03.003.
[4] Ridha M, Tan VBC, Tay TE. Traction-separation laws for progressive failure of bonded scarf repair of composite panel. Compos Struct 2011;93:1239–45. https://doi.org/10.1016/j.compstruct.2010.10.015.
[5] Whittingham B, Baker AA, Harman A, Bitton D. Micrographic studies on adhesively bonded scarf repairs to thick composite aircraft structure. Compos Pt A-Appl Sci Manuf 2009;40:1419–32. https://doi.org/10.1016/j.compositesa.2008.12.011.
[6] Hu FZ, Soutis C. Strength prediction of patch-repaired CFRP laminates loaded in compression. Compos Sci Technol 2000;60:1103–14. https://doi.org/10.1016/S0266-3538(00)00011-7.
[7] Soutis C, Hu FZ. Design and performance of bonded patch repairs of composite structures. Proc Inst Mech Eng Part G-J Aerosp Eng 1997;211:263–71. https://doi.org/10.1243/0954410971532668.
[8] Ramji M, Srilakshmi R, Bhanu Prakash M. Towards optimization of patch shape on the performance of bonded composite repair using FEM. Compos Pt B-Eng 2013;45:710–20. https://doi.org/10.1016/j.compositesb.2012.07.049.
[9] Cheng P, Gong XJ, Aivazzadeh S, Xiao X. Experimental observation of tensile behavior of patch repaired composites. Polym Test 2014;34:146–54. https://doi.org/10.1016/j.polymertesting.2014.01.007.
[10] Cheng P, Gong XJ, Hearn D, Aivazzadeh S. Tensile behaviour of patch-repaired CFRP laminates. Compos Struct 2011;93:582–9. https://doi.org/10.1016/j.compstruct.2010.08.021.
[11] Bhatia GS, Andrew JJ, Balaganesan G, Arockiarajan A. The role of patch-parent configurations on the tensile response of patch repaired carbon/epoxy laminates. Polym Test 2018;70:413–25. https://doi.org/10.1016/j.polymertesting.2018.07.025.
[12] Tanulia V, Wang J, Pearce GM, Baker A, Chang P, Prusty BG. Experimental and computational assessment of disbond growth and fatigue life of bonded joints and patch repairs for primary airframe structures. Int J Fatigue 2022;159:106776. https://doi.org/10.1016/j.ijfatigue.2022.106776.
[13] Li C, Zhao Q, Yuan J, Hou Y, Tie Y. Simulation and experiment on the effect of patch shape on adhesive repair of composite structures. J Compos Mater 2019;53:4125–35. https://doi.org/10.1177/0021998319853033.
[14] Gong X-J, Cheng P, Aivazzadeh S, Xiao X. Design and optimization of bonded patch repairs of laminated composite structures. Compos Struct 2015;123:292–300. https://doi.org/10.1016/j.compstruct.2014.12.048.
[15] Okafor AC, Singh N, Enemuoh UE, Rao SV. Design, analysis and performance of adhesively bonded composite patch repair of cracked aluminum aircraft panels. Compos Struct 2005;71:258–70. https://doi.org/10.1016/j.compstruct.2005.02.023.
[16] Rachid M, Serier B, Bouiadjra BB, Belhouari M. Numerical analysis of the patch shape effects on the performances of bonded composite repair in aircraft structures. Compos Pt B-Eng 2012;43:391–7. https://doi.org/10.1016/j.compositesb.2011.08.047.
[17] Benyahia F, Albedah A, Bouiadjra BB. Analysis of the adhesive damage for different patch shapes in bonded composite repair of aircraft structures. Mater Des 2014;54:18–24. https://doi.org/10.1016/j.matdes.2013.08.024.

[18] Kwon YW, Hall BL. Analyses of cracks in thick stiffened plates repaired with single-sided composite patch. Compos Struct 2015;119:727–37. https://doi.org/10.1016/j.compstruct.2014.09.052.

[19] Mohammadi S. The effect of disbond on the efficiency and durability of a composite patch repair in mode I and mixed mode considering different patch materials. Polym Polym Compos 2022;30. https://doi.org/10.1177/09673911211062759.

[20] Djebbar SC, Madani K, El Ajrami M, Houari A, Kaddouri N, Mokhtari M, et al. Substrate geometry effect on the strength of repaired plates: Combined XFEM and CZM approach. Int J Adhes Adhes 2022;119:103252. https://doi.org/10.1016/j.ijadhadh.2022.103252.

[21] Makwana AH, Vyas N, Barot RS. Numerical investigation of composite patch repair of inclined cracked panel using XFEM. Mater Today Proc 2021;45:5128–33. https://doi.org/10.1016/j.matpr.2021.01.643.

[22] Hart DC, Bruck HA. Predicting failure of cracked aluminum plates with one-sided composite patch. Int J Fract 2021;227:205–18. https://doi.org/10.1007/s10704-020-00509-4.

[23] Sarmah A, Dasari SS, Nagabandi N, Carey DG, Micci-Barreca SA, Vashisth A, et al. Patch repair of composites using Dielectric Barrier Discharge-induced heating and curing. Appl Mater Today 2023;32:101821. https://doi.org/10.1016/j.apmt.2023.101821.

[24] Jiang H, Ren Y. CFRP-patching enhancement on open-hole CFRP panel with micro/nanofillers-modified adhesive interface: Experimental and numerical simulation. Compos Sci Technol 2022;218:109180. https://doi.org/10.1016/j.compscitech.2021.109180.

[25] Ji X, Zhou W, Sun H, Liu J, Ma L. Damage evolution behavior of bi-adhesive repaired composites under bending load by acoustic emission and micro-CT. Compos Struct 2022;279:114742. https://doi.org/10.1016/j.compstruct.2021.114742.

[26] Li L, Liu W, Wang Y, Zhao Z. Mechanical performance and damage monitoring of CFRP thermoplastic laminates with an open hole repaired by 3D printed patches. Compos Struct 2023;303:116308. https://doi.org/10.1016/j.compstruct.2022.116308.

[27] Rashvand K, Eder MA, Sarhadi A. In-situ and adhesive repair of continuous fiber composites using 3D printing. Addit Manuf 2024;80:103975. https://doi.org/10.1016/j.addma.2024.103975.

[28] Kashfuddoja M, Ramji M. Assessment of local strain field in adhesive layer of an unsymmetrically repaired CFRP panel using digital image correlation. Int J Adhes Adhes 2015;57:57–69. https://doi.org/10.1016/j.ijadhadh.2014.10.005.

[29] Matta S, Kolanu NR, Chinthapenta V, Manjunatha CM, Ramji M. Progressive damage analysis of adhesively bonded patch repaired carbon fibre-reinforced polymer specimen under compression involving cohesive zone model. Int J Damage Mech 2019;28:1457–89. https://doi.org/10.1177/1056789519832062.

[30] Hall ZEC, Liu J, Brooks RA, Liu H, Crocker JWM, Joesbury AM, et al. The effectiveness of patch repairs to restore the impact properties of carbon-fibre reinforced-plastic composites. Eng Fract Mech 2022;270:108570. https://doi.org/10.1016/j.engfracmech.2022.108570.

[31] Liu H, Liu J, Hall ZEC, Brooks RA, Crocker JWM, Joesbury AM, et al. Modelling the effects of patch-plug configuration on the impact performance of patch-repaired composite laminates. Compos Sci Technol 2023;233:109917. https://doi.org/10.1016/j.compscitech.2023.109917.

[32] Sun Z, Pi X, Tie Y, Li C. Study on impact resistance and parameter optimization of patch-repaired plain woven composite based on multi-scale analysis. Polym Compos 2023;44:5087–103. https://doi.org/10.1002/pc.27474.

[33] Chen X, Peng Y, Wang K, Wang X, Liu Z, Huang Z, et al. Experimental and simulation study on bonded repaired low-velocity impact of carbon fiber reinforced plastic laminates for rail vehicles. J Mater Res Technol 2024;28:446–58. https://doi.org/10.1016/j.jmrt.2023.12.005.

[34] Clark RJ, Romilly DP. Linear coupled bending and extension of an unbalanced bonded repair. Int J Solids Struct 2007;44:3156–76. https://doi.org/10.1016/j.ijsolstr.2006.09.012.

[35] Bellali MA, Serier B, Mokhtari M, Campilho RDSG, Lebon F, Fekirini H. XFEM and CZM modeling to predict the repair damage by composite patch of aircraft structures: Debonding parameters. Compos Struct 2021;266:113805. https://doi.org/10.1016/j.compstruct.2021.113805.

[36] Abderahmane S, Mokhtar BM, Smail B, Wayne SF, Zhang L, Belabbes BB, et al. Experimental and numerical disbond localization analyses of a notched plate repaired with a CFRP patch. Struct Eng Mech 2017;63:361–70. https://doi.org/10.12989/sem.2017.63.3.361.

[37] Albedah A, Mohammed SMAK, Bouiadjra BB, Bouiadjra BAB, Benyahia F. Effect of the patch length on the effectiveness of one-sided bonded composite repair for aluminum panels. Int J Adhes Adhes 2018;81:83–9. https://doi.org/10.1016/j.ijadhadh.2017.11.012.

[38] Oterkus E, Barut A, Madenci E, Ambur DR. Nonlinear analysis of a composite panel with a cutout repaired by a bonded tapered composite patch. Int J Solids Struct 2005;42:5276–306. https://doi.org/10.1016/j.ijsolstr.2005.02.024.

[39] Librescu L, Song O. On the static aeroelastic tailoring of composite aircraft swept wings modelled as thin-walled beam structures. Compos Eng 1992;2:497–512. https://doi.org/10.1016/0961-9526(92)90039-9.

[40] Kumabe S, Yashiro S, Onodera S. Evaluation of the frictional effect on the energy release rate in doubly end-notched tension test for mode II delamination. Eng Fract Mech 2023;288:109354. https://doi.org/10.1016/j.engfracmech.2023.109354.

[41] Onodera S, Kawahara K, Yashiro S. Damage progression and strength prediction of open-hole CFRP laminates containing ply gaps. Eng Fract Mech 2023;293:109681. https://doi.org/10.1016/j.engfracmech.2023.109681.

[42] Oshima S, Yoshimura A, Yashiro S, Hirano Y, Ogasawara T. Experimental and analytical validation of mode II fracture toughness tests for a type of double-lap joint. Compos Struct 2020;234:111757. https://doi.org/10.1016/j.compstruct.2019.111757.

[43] Yashiro S, Wada J, Sakaida Y. A monitoring technique for disbond area in carbon fiber–reinforced polymer bonded joints using embedded fiber Bragg grating sensors: Development and experimental validation. Struct Health Monit 2017;16:185–201. https://doi.org/10.1177/1475921716669979.

[44] Nadabe T, Nishikawa M, Minakuchi S, Nakamura T, Siivola JT, Takeda N. Numerical analysis for damage detection in CFRP bolted joints using strain measurement. J Jpn Soc Compos Mater 2012;38:22–9. https://doi.org/10.6089/jscm.38.22. in Japanese.

[45] Sarfaraz R, Canal LP, Violakis G, Botsis J, Michaud V, Limberger HG. An experimental–numerical investigation of hydrothermal response in adhesively bonded composite structures. Compos Part A 2015;73:176–85. https://doi.org/10.1016/j.compositesa.2015.03.005.

[46] Ong WH, Rajic N, Chiu WK, Rosalie C. Adhesive material property evaluation for improved Lamb wave simulation. Int J Adhes Adhes 2016;71:28–38. https://doi.org/10.1016/j.ijadhadh.2016.08.008.

[47] Michopoulos JG, Apetre NA, Iliopoulos AP, Steuben JC. Effects of elastoplasticity, damage, and environmental exposure on the behavior of adhesive step-lap joints. J Comput Inf Sci Eng 2023;23:030904. https://doi.org/10.1115/1.4056361.

[48] Tsai SW, Hahn HT. Introduction to Composite Materials. Westport: Technomic; 1980.

[49] Bower AF. Applied Mechanics of Solids. Boca Raton: CRC Press; 2010.

[50] Asp LE, Berglund LA, Talreja R. A criterion for crack initiation in glassy polymers subjected to a composite-like stress state. Compos Sci Technol 1996;56:1291–301. https://doi.org/10.1016/S0266-3538(96)00090-5.

[51] Toray Industries, 2592 PREPREG SYSTEM. https://www.cf-composites.toray/ja/resources/data_sheets/pdf/datasheets_2592_2593.pdf (accessed 3 October 2024).

[52] Yashiro S, Ono R, Ogi K. Effect of machining conditions on the trimming damage in composite laminates induced by out-of-plane shearing. J Mater Process Technol 2019;271:463–75. https://doi.org/10.1016/j.jmatprotec.2019.04.025.

[53] Moutsompegka E, Tserpes K, Noeske M, Schlag M, Brune K. Experimental investigation of the effect of pre-bond contamination with fingerprints and ageing on the fracture toughness of composite bonded joints. Appl Compos Mater 2019;26:1001–19. https://doi.org/10.1007/s10443-019-09763-9.

[54] Damghani M, Bolanos S, Chahar A, Matthews J, Atkinson GA, Murphy A, et al. Design, novel quality check and experimental test of an original variable length stepped scarf repair scheme. Compos Part B 2022;230:109542. https://doi.org/10.1016/j.compositesb.2021.10954.